Check for updates

ADVANCED MATERIALS
www.advmat.de

Guided Mid-IR and Near-IR Light within a Hybrid Hyperbolic-Material/Silicon Waveguide Heterostructure

*Mingze He, Sami I. Halimi, Thomas G. Folland, Sai S. Sunku, Song Liu, James H. Edgar, D. N. Basov, Sharon M. Weiss, and Joshua D. Caldwell**

Silicon waveguides have enabled large-scale manipulation and processing of near-infrared optical signals on chip. Yet, expanding the bandwidth of guided waves to other frequencies will further increase the functionality of silicon as a photonics platform. Frequency multiplexing by integrating additional architectures is one approach to the problem, but this is challenging to design and integrate within the existing form factor due to scaling with the free-space wavelength. This paper demonstrates that a hexagonal boron nitride (hBN)/silicon hybrid waveguide can simultaneously enable dual-band operation at both mid-infrared (6.5–7.0 µm) and telecom (1.55 µm) frequencies, respectively. The device is realized via the lithography-free transfer of hBN onto a silicon waveguide, maintaining near-infrared operation. In addition, mid-infrared waveguiding of the hyperbolic phonon polaritons (HPhPs) supported in hBN is induced by the index contrast between the silicon waveguide and the surrounding air underneath the hBN, thereby eliminating the need for deleterious etching of the hyperbolic medium. The behavior of HPhP waveguiding in both straight and curved trajectories is validated within an analytical waveguide theoretical framework. This exemplifies a generalizable approach based on integrating hyperbolic media with silicon photonics for realizing frequency multiplexing in on-chip photonic systems.

The silicon waveguide, which transmits and routes optical signals, is the most indispensable building block in on-chip optical technologies for high-speed optical processing,[1,2] communications,[1,3–5] and chemical spectroscopy.[6] With demand for continuous increases in operational bandwidth, there is a desire to expand the operating frequency regime as multiplexing of near- and mid-infrared (mid-IR) signals could provide unique applications for both signal processing and chemical sensing simultaneously.[7] However, this is challenging with integrated silicon photonics, as accommodating longer wavelength modes requires expanding the silicon waveguide size,[7] causing severe modal dispersion in the near-IR.[8] Thus, an architecture that maintains the performance of the silicon waveguide in the near-IR, while providing confinement and propagation of mid-IR light at deeply subdiffractional length scales, but within the same form factor, would be highly beneficial.

Hyperbolic phonon polaritons (HPhPs)[9–12] can compress long-wavelength free-space light to deeply subdiffractional volumes and hence overcome the length-scale mismatch with structures designed for operation in the near-IR. Such HPhPs are supported within highly anisotropic media where the permittivity along orthogonal axes is opposite in sign,[13] with hyperbolicity being demonstrated in an expanding list of natural materials,[11,14–17] such as hexagonal boron nitride (hBN).[10] Guiding of HPhPs in hBN has been studied previously using patterned strips[18–20] and by introducing in-plane polaritonic refraction of HPhPs.[21,22] In the context of the former, hBN strips were constructed through nanofabrication and physical etching processes. However, such etching introduces unavoidable material damage,[9,18,23–25] increasing the loss and reducing the propagation length of the HPhPs. Further,

M. He, Prof. T. G. Folland, Prof. J. D. Caldwell
Department of Mechanical Engineering
Vanderbilt University
Nashville, TN 37212, USA
E-mail: josh.caldwell@vanderbilt.edu

S. I. Halimi, Prof. S. M. Weiss, Prof. J. D. Caldwell
Department of Electrical Engineering and Computer Science
Vanderbilt University
Nashville, TN 37212, USA

Prof. T. G. Folland
Department of Physics and Astronomy
The University of Iowa
Iowa City, IA 52242, USA

The ORCID identification number(s) for the author(s) of this article can be found under https://doi.org/10.1002/adma.202004305.

S. S. Sunku
Department of Physics
Columbia University
New York, NY 10027, USA

S. S. Sunku, Prof. D. N. Basov
Department of Applied Physics and Applied Mathematics
Columbia University
New York, NY 10027, USA

S. Liu, Prof. J. H. Edgar
Tim Taylor Department of Chemical Engineering
Kansas State University
Manhattan, KS 66506, USA

DOI: 10.1002/adma.202004305

 © 2021 Wiley-VCH GmbH

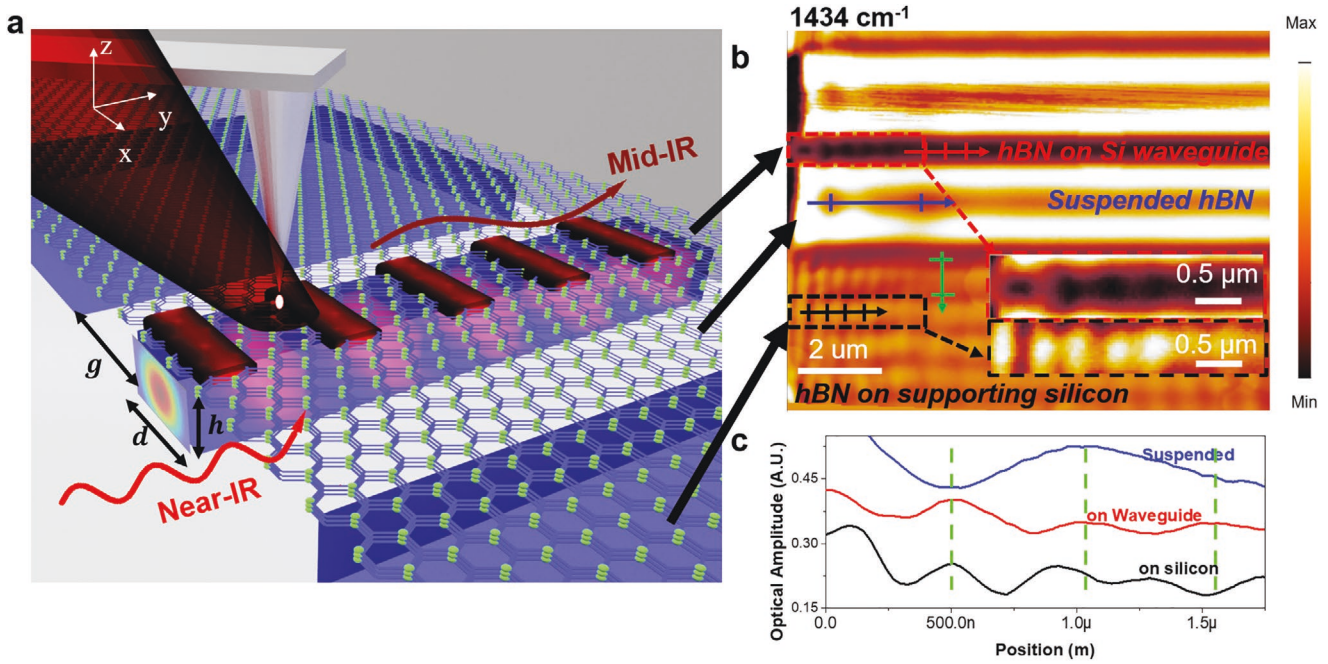

Figure 1. Waveguiding of light in the mid-IR and near-IR within the same device. a) Device and experimental schematics. The silicon regions are presented as transparent blue domains, with the gray substrate corresponding to silicon dioxide. The silicon waveguide is formed by etching away part of the silicon, with the h^{10}BN slab transferred on top, resulting in the h^{10}BN flake covering the waveguide region and the wider silicon supports, with h^{10}BN suspended between these silicon regions forming freestanding h^{10}BN domains (over air). The width (*d*) and height (*h*) of the silicon waveguide is 700 nm and 220 nm, respectively, and the gap (*g*) between the silicon waveguide and supporting silicon is 1.65 µm. The thickness of h^{10}BN (*t*) is 40 nm (73 nm) for the device in (b) (Figure 2), each of which features several layers of h^{10}BN—however, only three layers are drawn in the schematic for aesthetic reasons. HPhP-WG modes (dark red waves) are imaged by s-SNOM, while the transmission of near-IR light (pink modes in silicon) is not influenced, and the modal wavelengths of the two modes are nearly the same. b) s-SNOM amplitude image of h^{10}BN above a silicon waveguide at 1434 cm^{-1}, which shows the difference between HPhPs on unpatterned silicon region and HPhP-WG. The red arrow corresponds to the tip-launched HPhP-WG mode, the blue arrow to tip-launched HPhPs in suspended h^{10}BN, the black arrow for tip-launched HPhPs in h^{10}BN over silicon, and the green arrow represents an edge-launched HPhP in h^{10}BN above the unpatterned silicon. The inset s-SNOM images are zoomed in to more clearly present the fields associated with the HPhP-WG and HPhPs over silicon, respectively, with the same scale bar. c) Line scans of three different tip-launched HPhPs observed: HPhP-WG, HPhPs over silicon region, and HPhPs over suspended region. The line profiles are extracted from the corresponding regions shown in panel (b).

the guided modes supported in such a finite width system are Fabry-Perot modes in nature,[18] rather than consistent with a traditional dielectric waveguide mode. Thus, it is unlikely that such modes can be described via the framework of dielectric waveguide theory.[8] The latter approach uses inducing refractive effects in plane,[21,22] where the propagation of HPhPs over different substrates or domains in phase-change materials follows Snell's law (Section S1, Supporting Information). Therefore, the patterning of the underlying substrate can also be used to control HPhP propagation.[21,22] However, using phase change materials causes detrimental substrate absorption in the near-IR[21,22] that precludes their use as a waveguide medium in this spectral range. Thus, an architecture for frequency multiplexing of mid-IR and near-IR is yet to be demonstrated.

Here, we address this challenge by realizing guided mid-IR and near-IR light within a hybrid hyperbolic-material/silicon waveguide heterostructure (**Figure 1**a). By exploiting substrate-induced changes in polariton wavelength (the reciprocal of HPhP wavevector) and thus polaritonic refraction, we demonstrate that the type II HPhPs supported by an intact hBN slab can be confined laterally and guided by the underlying silicon waveguide structure. We stress that the silicon waveguide within this heterostructure can simultaneously support a near-IR waveguide mode. Using scattering-type scanning near-field optical microscopy (s-SNOM) in the mid-IR, we experimentally detected the HPhP waveguide (HPhP-WG) modes, with both fundamental and higher-order modes reported. We corroborate this by demonstrating strong quantitative agreement in the spectral dispersion and modal profiles with analytical waveguide theory. Additionally, we validate the waveguide nature of the HPhP-WG modes by demonstrating that they can propagate along nonlinear trajectories, following the structure of curved waveguides with diameters in excess of the polariton wavelengths as well. Finally, we experimentally demonstrate that the presence of the hBN slab results in a negligible influence on waveguiding of near-IR light, and thus, the prototype hybrid waveguide can operate in both the near- and mid-IR simultaneously. Such heterogeneous, yet simplified, integration offers a generalizable approach for multiplexing dramatically different free-space wavelength light within a compact and on-chip footprint, offering a new toolset for nanophotonic design that maintains the low-loss properties of natural hyperbolic materials.

Because the properties of hyperbolic refractive waveguides have not been explored in any substantive manner, we first construct a numerical model to present this phenomenon. To form a waveguide mode, two criteria must be satisfied: i) a high index

© 2021 Wiley-VCH GmbH

material surrounded by a low index material and ii) constructive interference of the optical mode. In our geometry, we have exfoliated and transferred hBN flakes onto prepatterned silicon waveguides, with the surrounding region consisting of areas where the silicon was etched, resulting in freely suspended hBN (Figure 1a). The high refractive index of silicon compared with air makes the HPhP wavevectors of hBN on silicon two- to six-times higher than that supported within suspended hBN within the upper Reststrahlen band (type II hyperbolic),[10,17,26,27] as shown in Section S1 (Supporting Information). As such, we have a polariton system featuring a high wavevector region surrounded by a low wavevector area, which is an analogy to a dielectric waveguide system with the high refractive index material inside low refractive index materials. To satisfy criterion (ii), we must use the wave equation and boundary conditions at the interface. The out-of-plane electric field (E_z) of the propagating HPhPs share the same form of the wave equation as nonpolariton supporting dielectric materials[10]

$$E_z = E_0\, e^{i(kr-\omega t)} \tag{1}$$

where E_0 is the amplitude, k is the HPhP wavevector, r is the position vector, ω is the frequency of the incident light, and t is time. Prior research has shown that the in-plane propagating hyperbolic waves follow Snell's law,[21,22] which implies the continuity of the tangential component of the HPhP wavevector. Because the propagating HPhPs share the same form of the wave equation, and presumably the same boundary conditions as dielectric materials, we anticipate that within our heterostructure design, a HPhP waveguide (HPhP-WG) mode confined to the x–y plane will result. As the electric field is along the z-direction, and in the presented configuration is propagating along the y-direction, we can treat the system as a TE dielectric slab waveguide. In detail, the HPhP-WG modes with a propagation constant, β, are the eigenvalues of the characteristic equation for the TE modes of a slab waveguide

$$\tan(\kappa d) = \frac{2\kappa\gamma}{\kappa^2 - \gamma^2} \tag{2}$$

where $\kappa = \sqrt{k_f{}^2 - \beta^2}$ and $\gamma = \sqrt{\beta^2 - k_s{}^2}$, and d is defined as the width of the underlying silicon waveguide (detailed HPhP-WG derivation is in Section S3, Supporting Information). Thus, the mid-IR HPhPs constrained within hBN (the z-axis) are also confined by the width of the waveguide region (the x-axis) and propagate parallel to the y-axis. Importantly, the presence of this mid-IR HPhP-WG mode does not influence the silicon waveguide underlying the hBN slab, and the near-IR light remains confined within the silicon cross section (x–z plane) and propagates along the y-axis, as shown schematically in Figure 1a. It is important to note that within the type I lower Reststrahlen band of hBN, the dispersion relation is inverted (see Section S15, Supporting Information) with respect to the type II upper band. Thus, such HPhP-WG modes would require a low substrate index "core" and high substrate index "cladding" (e.g., suspended hBN strip surrounded by hBN over a silicon field). However, such a structure cannot support a near-IR WG mode, eliminating the potential for the frequency multiplexing that is at the heart of this work.

To experimentally confirm the existence of HPhP-WG modes and contrast them with the widely studied HPhPs, we transferred a 40-nm-thick h^{10}BN flake onto a 0.7-μm-wide silicon waveguide (see optical images in Figure S4a, Supporting Information). Note that here we have used near monoisotopic h^{10}BN (^{10}B enriched to >99%), as this was shown previously to result in significantly reduced optical loss compared to naturally abundant hBN.[28] Once the prototype device was fabricated, we then used pseudo-heterodyne s-SNOM measurements at 1434 cm^{-1} (6.97 μm free-space wavelength) to measure the propagating HPhP-WG modes, as shown in Figure 1b. In this image, we can identify several tip- (black arrow) and edge-launched (green arrow) HPhPs over the unpatterned silicon regions, as well as tip-launched HPhPs in the suspended h^{10}BN domains (h^{10}BN over air, blue arrows). In addition to these different HPhPs, we also observe a tip-launched HPhP-WG mode (red arrow) confined within the h^{10}BN directly over the patterned silicon waveguide. To validate the HPhP-WG as a waveguide mode, line scans of the tip-launched HPhPs supported in h^{10}BN over the unpatterned silicon, suspended, and the silicon waveguide regions were extracted from Figure 1b and were plotted in Figure 1c. As anticipated for a waveguide mode, the wavevector over the waveguide region (propagation constant, notated as β) is smaller than the HPhP wavevectors over the continuous "core" silicon waveguide material (k_f), yet larger than the surrounding "cladding" material (k_s, HPhPs over the suspended region). This prediction can also be confirmed by inspection of the zoomed areas of interest in Figure 1b.

While the above-referenced prototype is suitable to identify the difference between HPhP-WG and HPhPs dictated by the substrate properties, this geometry most strongly stimulates tip-launched HPhPs. As such, the measured periodicity is halved HPhP wavelength,[10,29,30] making quantitative measurements more challenging due to the higher resolution that such detailed analysis requires. Therefore, to better characterize the HPhP-WG system, we fabricated additional silicon waveguides with a silicon-air edge (dashed line in **Figure 2**a, with additional scanning electron microscopy (SEM) images included in Figure S5, Supporting Information), and transferred a 73-nm-thick h^{10}BN flake on top (see the optical image in Figure S4, Supporting Information). This edge can efficiently scatter the incident mid-IR light, thus providing the necessary momentum to stimulate edge-launched HPhPs[21,28,31] into the waveguide. This enables direct observation of the HPhP-WG modes as shown in Figure 2b,d (see more s-SNOM images in Figure S15, Supporting Information). Here, near-field images were collected at various mid-IR frequencies, thereby enabling the HPhP-WG dispersion relation to be extracted and compared to analytical theory.

Although the HPhP-WG modes are conceptually visualized in the s-SNOM images, additional modal analysis is necessary for more comprehensive understanding and quantitative comparisons with theory. Accordingly, the cross-sectional line scans collected at 1450 and 1500 cm^{-1} are extracted and plotted against the calculated modal profile, as shown in Figure 2h,i. At 1450 cm^{-1}, we plot the inverted optical amplitude (a constant minus optical amplitude) to compensate for the influence of the hyperlensing effect, with the inverted line scan providing strong quantitative agreement with the

© 2021 Wiley-VCH GmbH

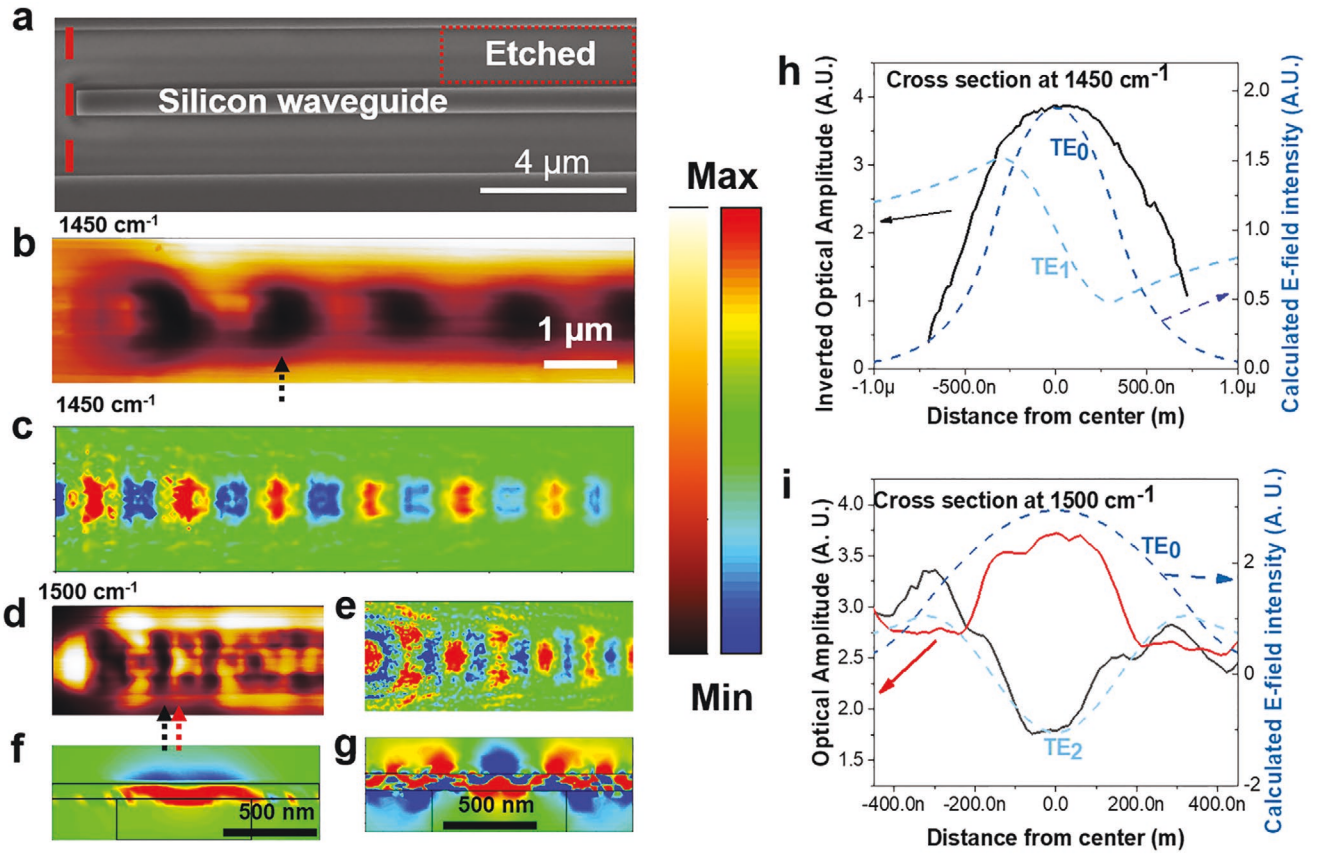

Figure 2. HPhP-WG mode analysis. a) SEM image of the silicon waveguide component in the heterostructure. The dashed line shows the edge of the waveguide, which is designed to launch HPhPs into the $h^{10}BN$ over the silicon waveguide. b) A near-field optical amplitude image of the HPhP-WG modes in $h^{10}BN$ over the silicon waveguide at 1450 cm^{-1}, c) with the corresponding spatial E_z distribution in the top view from the FEM simulations also provided. d,e) Corresponding near-field optical amplitude and FEM simulation plots of the same device measured at 1500 cm^{-1}, respectively. f,g) The cross-sectional field profiles from the FEM simulations at 1450 and 1500 cm^{-1} illustrate the TE_0 and TE_2 mode profiles, respectively. Panels (b)–(e) are at the same scale, and panels (f) and (g) are at the same scale. h,i) Cross-sectional line scans at different lateral positions of the waveguide at 1450 and 1500 cm^{-1}, respectively. The line profiles are plotted as solid lines, with the dashed arrows in (a) and (c) indicating the location where the line scans were extracted. The calculated mode profiles are plotted as dashed lines. To counter the hyperlensing effect at 1450 cm^{-1}, a constant minus the optical amplitude is plotted (more discussion in Section S6, Supporting Information).

analytically calculated fundamental waveguide TE modal profile (Figure 2h). Note that all s-SNOM images are influenced by the hyperlensing phenomenon, which is well studied in the literature,[32,33] with more related discussions concerning the impact of this effect upon our system provided in Section S6 (Supporting Information).

At higher frequencies, e.g., 1500 cm^{-1}, k_s (k_f) increases to 3.4×10^4 (1.1×10^5) cm^{-1}, and additional HPhP-WG modes become allowed. We propose that all allowed modes are excited and superimposed upon each other as HPhPs are launched into the waveguide via the silicon–air interface (dashed line in Figure 2a) without modal selectivity. We indeed discern two distinct cross-sectional profiles shown in Figure 2h, one that appears like the fundamental TE mode (TE_0) and another that exhibits a field profile similar to the second-order TE mode (TE_2). This second-order mode exhibits two peaks near the edge of the waveguide (Figure 2i), consistent with analytical solutions. Thus, we assign these HPhP-WG modes as TE_0 and TE_2, while the antisymmetric mode (TE_1) is not observed. In addition, the amplitude distribution of the modes can be revealed by analyzing line profiles along the waveguide,[18] and related discussion is included in Section S14 (Supporting Information).

To validate the experimental results in Figure 2b,d, we performed 3D finite element method (FEM) simulations to replicate the s-SNOM data. The simulated s-SNOM images show excellent agreement with experimental data, as shown in Figure 2c,e, with FEM simulations at additional frequencies provided in Section S7 (Supporting Information). From these FEM simulations, we extracted the cross-sectional field profiles, which also agree well with the analytically calculated modal profiles. Specifically, the field profiles at 1450 cm^{-1} only contain the mode exhibiting a single node, consistent with a TE_0 mode (Figure 2f), whereas at 1500 cm^{-1} an additional mode is detected with a field profile in good agreement with the TE_2 mode. Note that both FEM simulations and the s-SNOM images exhibit high symmetry, again confirming that the mode observed in experiments is consistent with the TE_2 HPhP-WG mode. TE_1 and TE_3 modes (and other odd modes) are not launched in our geometry due to the antisymmetric (Figure 2h) field profiles

© 2021 Wiley-VCH GmbH

of such odd modes, which are incompatible with HPhP-WGs launched by the symmetric waveguide edge (dashed line in Figure 2a). Although we do not detect these modes in either the FEM simulations of our experimental s-SNOM measurements, or the experimental results themselves, we do verify their existence using finite-difference time-domain (FDTD) simulations (Section S8, Supporting Information). Thus, we stress that there is no inherent reason why such odd-ordered HPhP-WG modes cannot be supported experimentally within other design geometries and/or using alternative excitation schemes.

While analyzing the s-SNOM images offers excellent qualitative agreement with both analytical calculations and FEM simulations, the wavevector analysis of the HPhP-WG modes is required to validate the degree of quantitative agreement. Predictive calculations of the HPhP-WG wavevectors are imperative for developing more advanced applications, such as understanding out-of-plane coupling in chemical sensing concepts and for the design of more complicated waveguide geometries, such as 1D photonic crystal structures. Therefore, here using the same analytical model, we calculate the propagation constant (β) of the allowed modes at each discrete frequency and plot these as the dashed lines in **Figure 3**. Similar to dielectric waveguides, at higher values of k_s and k_f (the accuracy of calculated k_f is validated by experimental data, see Section S2, Supporting Information), multiple HPhP-WG modes are potentially allowed. More specifically, while the TE_0 mode is always allowed in the upper Reststrahlen band of $h^{10}BN$, the onset of TE_1 is at 1445 cm^{-1}, and the TE_2 mode should occur at frequencies higher than 1495 cm^{-1}. By extracting the line profiles and fitting (details of fitting procedures are included in Section S9, Supporting Information), we extract the β of the HPhP-WG modes from the s-SNOM images (solid spheres). These extracted experimental β values are then compared to the analytical calculations (dashed lines) and FEM simulations (empty circles) in Figure 3. Consistent with our prior line scan analysis, we find that the dispersion of β is in excellent quantitative agreement with the analytically calculated TE_0 and TE_2 modes.

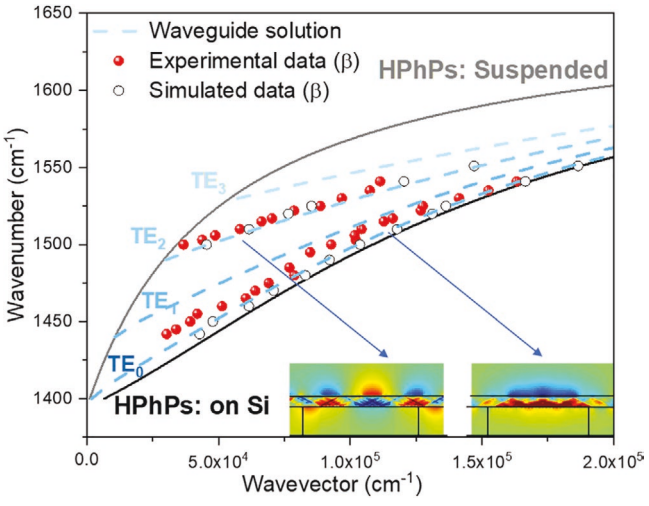

Figure 3. Dispersion curve of HPhP-WG modes. The experimental β are extracted from line scans of s-SNOM images and plotted as solid spheres, and the simulated β are extracted in the same manner from FEM simulations and plotted as empty circles. The dashed lines represent the analytically calculated mode solutions, with the solid lines corresponding to calculated dispersions of HPhPs in $h^{10}BN$ over silicon and suspended regions, respectively. Two mode profiles calculated via mode solver in FDTD at 1500 cm^{-1} are provided as insets.

Although the HPhP-WG is propagating mid-IR light with a free-space wavelength on the order of 7 μm, the propagation constant (β) of the deeply subdiffractional HPhP-WG is comparable to that of the guided near-IR modes in the silicon waveguide ($\beta_{HPhP} \approx \beta_{Si} \approx 1 \times 10^5$ cm^{-1}). This choice implies that the HPhP-WG in the mid-IR can be designed to share the propagation and modal characteristics with the silicon waveguide modes. The low group velocity and intrinsic material absorption of $h^{10}BN$ certainly result in shorter propagation lengths than the near-IR silicon waveguide modes, with the experimental values observed here limited to 4.5 μm (Section S10, Supporting Information). However, theoretically for an optimal thickness $h^{10}BN$ slab free of impurities,[28,34] the propagation length could be increased to 17–25 μm, with details of these predictions provided in Section S10 (Supporting Information). While the propagation length is not comparable to that of the near-IR components, its incorporation into the design demonstrates a potential means for frequency multiplexing for applications that do not require ultralong propagation lengths, such as environmental or chemical sensing.[35] Furthermore, this offers a generalized approach toward expanding the operating frequency to any regime where hyperbolic media can be realized with reasonably low optical losses. Even restricting operation to the use of $h^{10}BN$ for mid-IR frequencies, this platform offers significant opportunities for lab-on-a-chip approaches due to the spectral overlap of the upper Reststrahlen band with the chemical vibrational fingerprint range. Such an overlap can be exploited through the introduction of the surface-enhanced infrared absorption (SEIRA),[36,37] strong-coupling,[35,38,39] or refractive index sensing[40] modalities into the device design.

In on-chip photonics, light must also be able to propagate around bends with varying degrees of curvature to route and process optical signals within highly compact form factors. To demonstrate that HPhP-WG modes are capable of such behavior, we have also investigated curved waveguides. Here, the width of the curved waveguide was 0.6 μm, with a break in the ring structure included serving as a launching point for the edge-launched HPhPs. We fabricated structures featuring subwavelength inner diameters of 2, 4, and 6 μm to demonstrate propagation around different curvatures (**Figure 4**b inset and additional SEM images in Section S5, Supporting Information). A single 130-nm-thick $h^{10}BN$ flake was transferred[41] over all three ring waveguides (see the optical image in Figure S4c, Supporting Information), so the data from these structures could be compared directly, without variations in the HPhP dispersion induced by variations in $h^{10}BN$ thickness.[10,17,42] Again, we use s-SNOM to characterize these waveguides and show that the HPhPs are indeed guided along the curved trajectories, with representative behavior for all three structures provided in Figure 4a–c using an incident frequency of 1542 cm^{-1}. This guiding behavior is even maintained for ring diameters and waveguide widths that are over three and ten times smaller, respectively, than the free-space wavelength (λ_{FS} = 6.49 μm), as they are still larger than the deeply subdiffractional HPhP wavelengths (0.35–1.3 μm) at

© 2021 Wiley-VCH GmbH

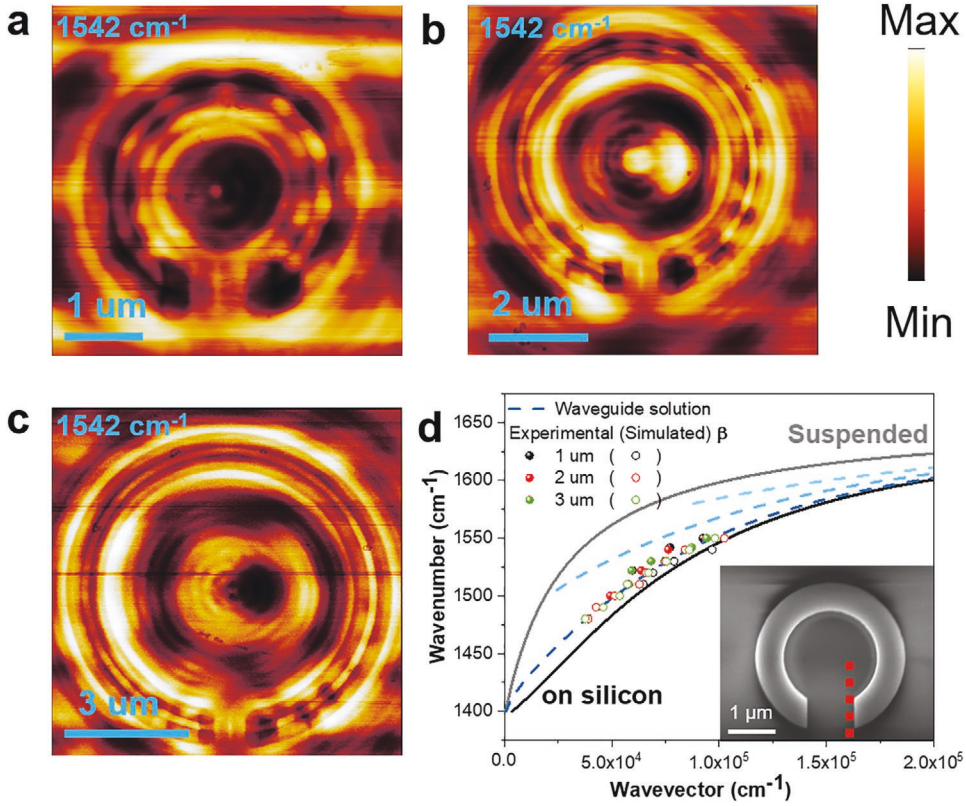

Figure 4. HPhP-WG modes in curved structures. a–c) Near-field optical amplitude images of $h^{10}BN$ on curved silicon waveguide structures at 1542 cm^{-1}. While the widths of the waveguide are the same (0.6 μm), the inner radii of the three structures are 1, 2, and 3 μm, respectively. d) Dispersion of the HPhP-WG modes for the curved structures with different radii. The experimentally extracted data are plotted as solid spheres, and the simulated β as open circles. The dashed lines are analytical solutions of slab waveguide model, and solid lines are calculated for $h^{10}BN$ HPhPs over silicon and in suspended $h^{10}BN$, respectively. A representative SEM image of a curved waveguide is provided as an inset.

this same incident frequency. Note that all of the curved edges of the waveguide can also launch HPhPs, like the silicon edge designed for the linear waveguides (dashed line in Figure 4d inset); thus, some localized HPhPs are also observed. However, in advanced designs, e.g., those featuring a grating coupler, such localized modes would not be induced as there would no longer be a coherent light irradiating the full curved waveguide structure.

To ensure that the modes in the curved waveguides are indeed HPhP-WGs, we again compare the spectral dispersion of the analytically calculated β with the values extracted from the s-SNOM experiments (Figure 4d). Although the β for the TE_0 modes extracted from different radii waveguides vary slightly from each other, the agreement of all extracted wavevectors with the analytical calculations remains excellent. Thus, these modes are consistent with the HPhP-WG modes described above, thereby validating the potential for routing mid-IR optical signals on-chip, even around bends within the same frequency multiplexed design. This demonstrates the possibility of integrating this approach with designs relying on such curved architectures, for instance, ring resonators and Mach–Zehnder interferometers.

The ability to guide mid-IR light through our hybrid HPhP-silicon waveguide platform creates opportunities for frequency multiplexing that could significantly expand operational bandwidth in on-chip silicon photonic approaches. However, while the HPhP-WG modes can indeed propagate along both straight and curved trajectories, this is only useful if the presence of the hyperbolic material is benign toward the near-IR operation. Because $h^{10}BN$ possesses a low refractive index in the near-IR and is a wide-bandgap semiconductor,[43] the effect of $h^{10}BN$ on the silicon photonics platform at 1.55 μm is anticipated to be minimal. To confirm this, we use an electromagnetic eigenmode solver to determine the various allowed modes within a 0.7-μm-wide silicon waveguide on silicon-on-insulator (SOI), with the primary guided modes presented in **Figure 5**a,b (more allowed modes are included in Section S11, Supporting Information). Repeating these calculations for the waveguide covered with a 50-nm-thick $h^{10}BN$ confirms that the presence of the $h^{10}BN$ has minimal impact upon the profiles of the two guided modes. More specifically, the effective modal index is changed by 2.0% (5.0%) for the zeroth (first) mode, as shown in Figure 5c,d. The system bears negligible intrinsic optical loss in the near-IR, with ≈0 dB cm^{-1} loss simulated for the guided mode of the silicon waveguide, both with and without hBN, from Lumerical MODE solutions. Experimentally, ref. [44] shows that the typical loss of a silicon strip waveguide is ≈4 dB cm^{-1} due to fabrication imperfection, and a similar level of loss is expected in our heterostructure in the near-IR.

© 2021 Wiley-VCH GmbH

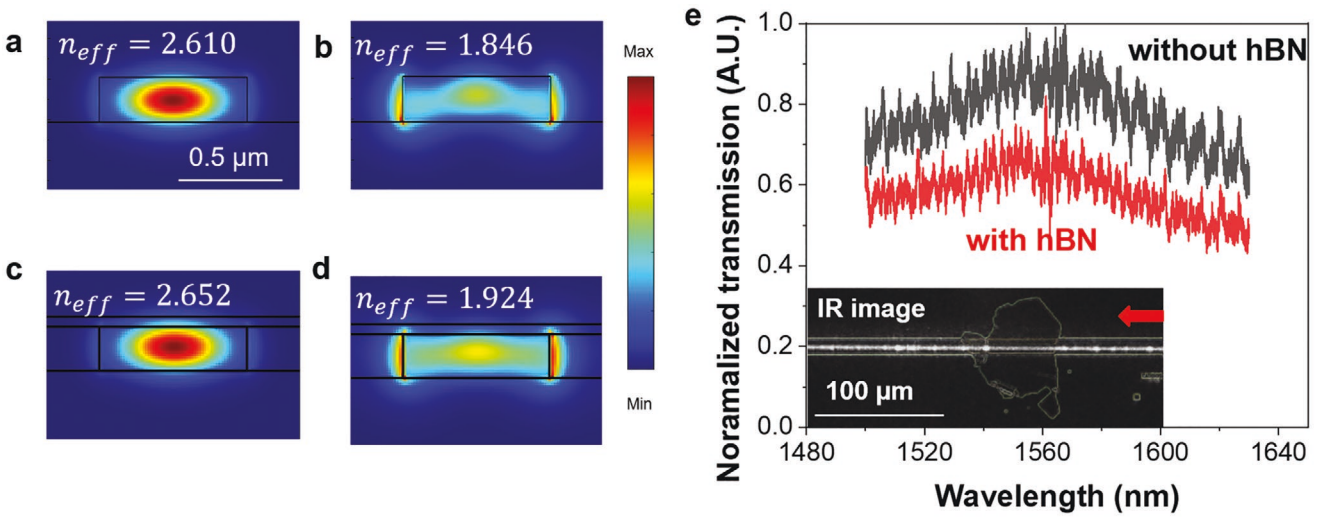

Figure 5. Performance of the hybrid system in the near-IR. Mode profiles (intensity of electrical field) at 1550 nm for zeroth- and first-order modes in a silicon waveguide a,b) without $h^{10}BN$ and c,d) with $h^{10}BN$ on top. All mode profiles here are at the same geometrical scale bar. e) Measured transmission spectrum before and after $h^{10}BN$ was transferred onto the silicon waveguide. The left inset shows an infrared camera image of a segment of the waveguide partly covered by a $h^{10}BN$ flake, with light coupled in from a tunable laser (red arrow indicates the input port), and the image is overlaid with the edge of the $h^{10}BN$ extracted from a visible image to show the position of $h^{10}BN$.

To experimentally validate the performance of the heterostructure in the near-IR, $h^{10}BN$ flakes were transferred onto a silicon waveguide sample, and the transmission intensity was measured before and after the $h^{10}BN$ was transferred (Figure 5e). Although we see immeasurable changes from simulations (Figure S12, Supporting Information), the transmission of the silicon waveguide partly covered with $h^{10}BN$ is reduced slightly. Because $h^{10}BN$ is lossless in the near-IR, the only way that $h^{10}BN$ influences the transmission is to induce reflection and/or scattering at the edges of $h^{10}BN$. To determine the severity of such scattering, we collected near-IR images while near-IR light was propagating within the waveguide. The near-IR camera image is overlaid with the edge of $h^{10}BN$ extracted from the visible image to illustrate the positioning of the $h^{10}BN$ flake, as shown in the inset of Figure 5e (raw data are included in Section S12, Supporting Information). Even though we see significant scattering on the waveguide that could be caused by wear of the chip or surface roughness, the scattering where the light enters the $h^{10}BN$/waveguide region is negligible, which is consistent with simulations (Figure S12, Supporting Information). Thus, we attribute the reduction in transmission intensity to minor degradation of the chip during handling and a possible slight variation in coupling efficiency for the two measurements rather than the presence of $h^{10}BN$. We believe that a pristine $h^{10}BN$ layer on top of such a silicon waveguide would negligibly impact the near-IR performance, consistent with simulations.

In summary, we have demonstrated a novel approach for frequency multiplexing of near-IR and mid-IR signals through a hybrid, hyperbolic-silicon photonic waveguide platform. Within this geometry, we have illustrated that two disparate frequencies of light can be guided within the same structure with comparable wavevectors, despite drastically different free-space wavelengths in the near- and mid-IR. Benefitting from the nature of HPhPs, which strongly confines light to deeply subdiffractional volumes, yet remains sensitive to the local refractive index, the utilization of the patterned substrates to create HPhP-WGs in $h^{10}BN$ becomes possible. We demonstrate that both the fundamental and high-order HPhP-WG modes can be supported within a 0.7-μm-wide $h^{10}BN$/silicon heterostructure without patterning the $h^{10}BN$, despite a free-space wavelength that is ≈10 times larger than the waveguide width. Moreover, we show that these HPhP-WG modes can be routed on-chip, exhibiting propagation around bends featuring radii sixfold smaller than the free-space wavelength, yet significantly larger than the guided HPhP wavelength, further illustrating its utility for on-chip photonics. Finally, these HPhP-WG modes in the mid-IR can in principle be supported simultaneously with the silicon waveguide modes in the near-IR, as the presence of the $h^{10}BN$ exhibits negligible impact upon near-IR light propagation for pristine samples. This therefore uncovers a potential generalizable solution for expanding operational bandwidth with minimal cross-talk due to the large spectral mismatch between signals, but within a single nanoscale integrated platform. Moreover, this approach benefits from exploiting the underlying waveguides patterned into the substrate rather than the etching of the hyperbolic material itself, thereby offering a general method for manipulating HPhPs without deleterious increases in loss resulting from such etching processes.

Experimental Section

Device Fabrication: All the silicon waveguides were fabricated on a SOI wafer with a 220 nm silicon device layer and a 3 μm buried oxide layer. The structures were patterned with standard nanofabrication procedures, using electron beam lithography (JEOL 9300FS) and reactive ion etching (Oxford Plasmalab 100) with a $C_4F_8/SF_6/Ar$ gas mixture to define the waveguide geometries. The aforementioned lithography steps were performed at the Center for Nanophase Materials Sciences at Oak Ridge National Laboratory. For mid-IR operation, ^{10}B enriched hBN

© 2021 Wiley-VCH GmbH

(≈99% enriched[28,45]) flakes were exfoliated and transferred onto the prepatterned SOI silicon waveguides using low contamination transfer techniques. The h^{10}BN crystals were grown with a boron source that was nearly 100% ^{10}B isotope, as previously described.[46]

Numerical Simulations: 3D FEM simulations in the mid-IR were conducted in CST Studio Suite 2018 using the frequency domain solver with open boundary conditions. In these simulations, polariton modes were only launched by a current point dipole above h^{10}BN, and field profiles were extracted using frequency monitors. All results used thicknesses consistent with that measured in topographic maps of the samples. The mode solutions for the HPhP-WG in the mid-IR were performed using the mode solver in Lumerical FDTD, and FDTD simulations in the mid-IR were performed using Lumerical FDTD. Modes for the silicon waveguides were calculated in the near-IR in Lumerical MODE Solutions using a finite-difference eigenmode solver. Dielectric functions of isotopically enriched h^{10}BN in the mid-IR were taken from ref. [28], and tabulated values can be found at Caldwell group website.[47] The dielectric function of h^{10}BN was taken in the near-IR from ref. [43]: the in-plane (x–y plane) permittivity is $4.41 + 0i$ and the out-of-plane (z-axis) permittivity is $3.24 + 0i$ at 1550 nm. For the dielectric function of silicon, the default values were used in Lumerical and CST STUDIO for near- and mid-IR, respectively, which is "Palik silicon"[48] ($12.075 + 0i$ at 1550 nm) and a constant ($11.9 + 0i$ in the mid-IR), respectively.

Near-Field Measurements: Near-field nano-imaging experiments were carried out in a commercial (www.neaspec.com) s-SNOM based around a tapping-mode atomic force microscope. A metal-coated Si tip of apex radius $R \approx 20$ nm that oscillates at a frequency of $\Omega \approx 280$ kHz and tapping amplitude of about 100 nm was illuminated by a monochromatic quantum cascade laser beam at a free-space incident wavelength $\lambda = 6.9$ µm and at an angle 60° off normal to the sample surface, with the incident light being p-polarized. Because s-SNOM predominantly couples to p-polarized component, the signal detected is dominated by HPhP signals, which can only emerge from p-polarized light.[49] Scattered light launches HPhPs in the device and the tip then rescatters light (described more completely in the main text) for detection in the far-field. Similar to previous studies of HPhPs using s-SNOM, the presence of the metallic tip will lead to the presence of a tip-launched mode. Background signals were efficiently suppressed by demodulating the detector signal at the third harmonic of the tip oscillation frequency and using pseudo-heterodyne interferometric detection. In s-SNOM images, HPhPs can be observed in two ways: first, polaritons launched by light scattered from the s-SNOM tip propagate radially away from the tip and reflect back from sample boundaries (e.g., a flake edge) creating interference fringes with spacing $\lambda_{HPhP}/2$,[10,29,30] which are scattered back to free space by the tip and detected. Alternatively, polaritons can be directly launched from the edge of patterned silicon structures under h^{10}BN or the edge of the h^{10}BN flake and then propagate across the surface and interfere with the incident field at the tip, producing fringes with spacing λ_{HPhP}.[21,28,31] The incident laser is aligned to be parallel to the waveguide to maximize the edge-launched HPhPs.

Near-IR Measurements: The near-IR propagation characteristics were measured using TE-polarized light (electric field polarized across the waveguide) from a tunable semiconductor laser source that was end-fire coupled into the waveguides through tapered fibers. The transmission intensity, captured by a fiber-coupled optical power meter, demonstrates some reduction in transmitted power after the transfer of an h^{10}BN flake atop the sample, likely due to handling-induced wear.

Supporting Information

Supporting Information is available from the Wiley Online Library or from the author.

Acknowledgements

M.H. and T.G.F. were supported by the Office of Naval Research under Grant No. N00014-18-1-2107 and via Vanderbilt University through J.D.C's startup package. J.D.C. was supported by the National Science Foundation (DMR1904793). Exfoliation and transfer of hBN were performed within the Vanderbilt Institute of Nanoscale Science and Engineering (VINSE) cleanroom, whereas silicon waveguide fabrication was conducted at the Center for Nanophase Materials Science, which is a DOE Office of Science User Facility. S.M.W. and S.I.H. were supported in part by the National Science Foundation (ECCS1809937). D.N.B. and S.S. were supported by the ONR-N000014-18-1-2722, and D.N.B. is the Vannevar Bush Faculty Fellow (ONR-VB: N00014-19-1-2630). The development of nano-imaging capabilities at Columbia is supported as part of Programmable Quantum Materials, an Energy Frontier Research Center funded by the U.S. Department of Energy (DOE), Office of Science, Basic Energy Sciences (BES), under award DE-SC0019443. S.L. and J.H.E. were supported by Materials Engineering and Processing program of the National Science Foundation (Grant No. CMMI 1538127).

Conflict of Interest

The authors declare no conflict of interest.

Keywords

heterostructure, hexagonal boron nitride, hyperbolic phonon polaritons, silicon waveguide

Received: June 24, 2020
Revised: November 28, 2020
Published online: February 1, 2021

[1] A. E. Willner, S. Khaleghi, M. R. Chitgarha, O. F. Yilmaz, *J. Lightwave Technol.* **2013**, *32*, 660.
[2] G. T. Reed, G. Mashanovich, F. Y. Gardes, D. Thomson, *Nat. Photonics* **2010**, *4*, 518.
[3] D. Patterson, I. De Sousa, L.-M. Achard, *Chip Scale Rev.* **2017**, 21.
[4] S. Thomas, K. Y. Bastardo, M. K. Anselm, presented at 2017 Pan Pacific Microelectronics Symp. (Pan Pacific), Kauai, Hawaii, February **2017**.
[5] P. Cheben, R. Halir, J. H. Schmid, H. A. Atwater, D. R. Smith, *Nature* **2018**, *560*, 565.
[6] M. C. Estevez, M. Alvarez, L. M. Lechuga, *Laser Photonics Rev.* **2012**, *6*, 463.
[7] Y. Zou, S. Chakravarty, C.-J. Chung, X. Xu, R. T. Chen, *Photonics Res.* **2018**, *6*, 254.
[8] A. W. Snyder, J. Love, *Optical Waveguide Theory*, Springer Science & Business Media, Berlin **2012**.
[9] J. D. Caldwell, A. V. Kretinin, Y. Chen, V. Giannini, M. M. Fogler, Y. Francescato, C. T. Ellis, J. G. Tischler, C. R. Woods, A. J. Giles, *Nat. Commun.* **2014**, *5*, 5221.
[10] S. Dai, Z. Fei, Q. Ma, A. Rodin, M. Wagner, A. McLeod, M. Liu, W. Gannett, W. Regan, K. Watanabe, D. N. Basov, *Science* **2014**, *343*, 1125.
[11] J. Sun, N. M. Litchinitser, J. Zhou, *ACS Photonics* **2014**, *1*, 293.
[12] K. Korzeb, M. Gajc, D. A. Pawlak, *Opt. Express* **2015**, *23*, 25406.
[13] A. Poddubny, I. Iorsh, P. Belov, Y. Kivshar, *Nat. Photonics* **2013**, *7*, 948.
[14] G. Álvarez-Pérez, T. G. Folland, I. Errea, J. Taboada-Gutiérrez, J. Duan, J. Martín-Sánchez, A. I. Tresguerres-Mata, J. R. Matson, A. Bylinkin, M. He, *Adv. Mater.* **2020**, *32*, 1908176.
[15] J. Taboada-Gutiérrez, G. Álvarez-Pérez, J. Duan, W. Ma, K. Crowley, I. Prieto, A. Bylinkin, M. Autore, H. Volkova, K. Kimura, *Nat. Mater.* **2020**, *19*, 964.
[16] R. R. da Silva, R. M. da Silva, T. Dumelow, J. da Costa, S. Honorato, A. Ayala, *Phys. Rev. Lett.* **2010**, *105*, 163903.
[17] J. D. Caldwell, I. Aharonovich, G. Cassabois, J. H. Edgar, B. Gil, D. Basov, *Nat. Rev. Mater.* **2019**, *4*, 552.

 © 2021 Wiley-VCH GmbH

[18] I. Dolado, F. J. Alfaro-Mozaz, P. Li, E. Nikulina, A. Bylinkin, S. Liu, J. H. Edgar, F. Casanova, L. E. Hueso, P. Alonso-González, *Adv. Mater.* **2020**, *5*, 1906530.
[19] V. E. Babicheva, M. Y. Shalaginov, S. Ishii, A. Boltasseva, A. V. Kildishev, *Opt. Express* **2015**, *23*, 31109.
[20] C. Maissen, I. D. Lopez, R. Hillenbrand, presented at 2017 42nd Int. Conf. Infrared, Millimeter, and Terahertz Waves (IRMMW-THz), Cancun, Mexico, August **2017**.
[21] T. G. Folland, A. Fali, S. T. White, J. R. Matson, S. Liu, N. A. Aghamiri, J. H. Edgar, R. F. Haglund, Y. Abate, J. D. Caldwell, *Nat. Commun.* **2018**, *9*, 4371.
[22] K. Chaudhary, M. Tamagnone, X. Yin, C. M. Spägele, S. L. Oscurato, J. Li, C. Persch, R. Li, N. A. Rubin, L. A. Jauregui, *Nat. Commun.* **2019**, *10*, 4487.
[23] A. J. Giles, S. Dai, O. J. Glembocki, A. V. Kretinin, Z. Sun, C. T. Ellis, J. G. Tischler, T. Taniguchi, K. Watanabe, M. M. Fogler, *Nano Lett.* **2016**, *16*, 3858.
[24] F. Alfaro-Mozaz, P. Alonso-González, S. Vélez, I. Dolado, M. Autore, S. Mastel, F. Casanova, L. Hueso, P. Li, A. Y. Nikitin, *Nat. Commun.* **2017**, *8*, 15624.
[25] P. Li, I. Dolado, F. J. Alfaro-Mozaz, F. Casanova, L. E. Hueso, S. Liu, J. H. Edgar, A. Y. Nikitin, S. Vélez, R. Hillenbrand, *Science* **2018**, *359*, 892.
[26] J. D. Caldwell, A. Kretinin, Y. Chen, V. Giannini, M. M. Fogler, Y. Francescato, C. Ellis, J. G. Tischler, C. Woods, A. J. Giles, M. Hong, K. Watanabe, T. Taniguchi, S. A. Maier, K. S. Novoselov, *Nat. Commun.* **2014**, *5*, 5221.
[27] S. Dai, J. Quan, G. Hu, C.-W. Qiu, T. H. Tao, X. Li, A. Alù, *Nano Lett.* **2018**, *19*, 1009.
[28] A. J. Giles, S. Dai, I. Vurgaftman, T. Hoffman, S. Liu, L. Lindsay, C. T. Ellis, N. Assefa, I. Chatzakis, T. L. Reinecke, *Nat. Mater.* **2018**, *17*, 134.
[29] Z. Fei, A. Rodin, G. O. Andreev, W. Bao, A. McLeod, M. Wagner, L. Zhang, Z. Zhao, M. Thiemens, G. Dominguez, *Nature* **2012**, *487*, 82.
[30] J. Chen, M. Badioli, P. Alonso-González, S. Thongrattanasiri, F. Huth, J. Osmond, M. Spasenović, A. Centeno, A. Pesquera, P. Godignon, *Nature* **2012**, *487*, 77.
[31] S. Dai, Q. Ma, Y. Yang, J. Rosenfeld, M. D. Goldflam, A. McLeod, Z. Sun, T. I. Andersen, Z. Fei, M. Liu, *Nano Lett.* **2017**, *17*, 5285.
[32] S. Dai, Q. Ma, T. Andersen, A. S. McLeod, Z. Fei, M. K. Liu, M. Wagner, K. Watanabe, T. Taniguchi, M. Thiemens, F. Keilmann, P. Jarillo-Herrero, M. M. Fogler, D. N. Basov, *Nat. Commun.* **2015**, *6*, 6963.
[33] P. Li, M. Lewin, A. V. Kretinin, J. D. Caldwell, K. S. Novoselov, T. Taniguchi, K. Watanabe, F. Gaussmann, T. Taubner, *Nat. Commun.* **2015**, *6*, 7507.
[34] R. Cuscó, J. H. Edgar, S. Liu, J. Li, L. Artús, *Phys. Rev. Lett.* **2020**, *124*, 167402.
[35] A. Bylinkin, M. Schnell, F. Calavalle, P. Li, J. Taboada-Gutitierrez, S. Liu, J. H. Edgar, F. Casanova, L. E. Hueso, P. Alonso-Gonzalez, *Nat. Photonics.* **2020**, 1.
[36] D. Yoo, D. A. Mohr, F. Vidal-Codina, A. John-Herpin, M. Jo, S. Kim, J. Matson, J. D. Caldwell, H. Jeon, N.-C. Nguyen, *Nano Lett.* **2018**, *18*, 1930.
[37] M. Autore, P. Li, I. Dolado, F. J. Alfaro-Mozaz, R. Esteban, A. Atxabal, F. Casanova, L. E. Hueso, P. Alonso-González, J. Aizpurua, A. Y. Nikitin, S. Vélez, R. Hillenbrand, *Light: Sci. Appl.* **2018**, *7*, 17172.
[38] T. G. Folland, G. Lu, A. Bruncz, J. R. Nolen, M. Tadjer, J. D. Caldwell, *ACS Photonics* **2020**, *7*, 614.
[39] R. Berte, C. R. Gubbin, V. D. Wheeler, A. J. Giles, V. Giannini, S. A. Maier, S. De Liberato, J. D. Caldwell, *ACS Photonics* **2018**, *5*, 2807.
[40] B. NeunerIII, D. Korobkin, C. Fietz, D. Carole, G. Ferro, G. Shvets, *J. Phys. Chem. C* **2010**, *114*, 7489.
[41] A. Kretinin, Y. Cao, J. Tu, G. Yu, R. Jalil, K. Novoselov, S. Haigh, A. Gholinia, A. Mishchenko, M. Lozada, *Nano Lett.* **2014**, *14*, 3270.
[42] A. Fali, S. T. White, T. G. Folland, M. He, N. A. Aghamiri, S. Liu, J. H. Edgar, J. D. Caldwell, R. F. Haglund, Y. Abate, *Nano Lett.* **2019**, *19*, 7725.
[43] Y. Rah, Y. Jin, S. Kim, K. Yu, *Opt. Lett.* **2019**, *44*, 3797.
[44] Y. A. Vlasov, S. McNab, *Opt. Express* **2004**, *12*, 1622.
[45] T. Vuong, S. Liu, A. Van der Lee, R. Cuscó, L. Artús, T. Michel, P. Valvin, J. Edgar, G. Cassabois, B. Gil, *Nat. Mater.* **2018**, *17*, 152.
[46] S. Liu, R. He, L. Xue, J. Li, B. Liu, J. H. Edgar, *Chem. Mater.* **2018**, *30*, 6222.
[47] https://my.vanderbilt.edu/caldwellgroup/dielectric-functions/ (accessed: January 2021).
[48] E. D. Palik, *Handbook of Optical Constants of Solids*, Vol. *3*, Academic, San Diego, CA **1998**.
[49] S. Foteinopoulou, G. C. R. Devarapu, G. S. Subramania, S. Krishna, D. Wasserman, *Nanophotonics* **2019**, *8*, 2129.

© 2021 Wiley-VCH GmbH